Optimisation of a dynamic absorber with nonlinear stiffness and damping for the vibration control of a toy model for floating offshore wind turbine

Pierre-Olivier Mattei, Renaud Côte

Optimisation of a dynamic absorber with nonlinear stiffness and damping for the vibration control of a toy model for floating offshore wind turbine

Pierre-Olivier Mattei[1] and Renaud Côte[1]

[1] Aix Marseille Univ, CNRS, Centrale Marseille, LMA UMR 7031, 4 impasse Nikola Tesla, CS 40006,13453 Marseille Cedex 13, France

Passive vibration mitigation of offshore wind turbines using nonlinear absorber or nonlinear energy sink has started to receive attention in the literature. In most case, little attention had been made on the possibility of detached resonance occurring when nonlinear energy sink is attached to the linear system describing the wind turbine. Sea movements that alter the initial conditions of the floating offshore wind turbine can lead to the nonlinear energy sink operating on one or more detached resonances that completely negate its ability to control turbine vibration. In this paper, we are interested in optimizing the parameters of a nonlinear energy sink with nonlinear stiffness and nonlinear viscous damping for the vibration control of a toy model (say a linear mass-stiffener-damper system) of a floating offshore wind turbine over its entire operating range. The mechanism of cancellation of the detached resonance is studied analytically under 1:1 resonance. It is shown that the nonlinear energy sink with a properly tuned nonlinear viscous damping allow the complete elimination of undesired regimes and completely restores the absorber ability to strongly limit floating offshore wind turbine vibration over its whole forcing range. The results obtained over a large domain of parameters suggest that both nonlinear energy sink optimal parameter (linear and nonlinear stiffness and nonlinear damping) and attenuation of floating offshore wind turbine vibratory motion depend upon simple power laws of nonlinear energy sink mass and linear damping.

Keywords Passive vibration reduction, nonlinear energy sink, geometrically nonlinear damping, floating offshore wind turbine.

1 Introduction

Wind renewable energy is rapidly developing nowadays. Offshore wind turbines are particularly adapted to generate high power in various environmental condition. They are, in fact, subject to more regular wind conditions than in the middle of the land and to the possibility of developing large wind turbines which are more efficient from the energy point of view, by using slender towers and extremely long blades, and less disturbing for the local residents and the fauna. Among these, floating offshore wind turbines (FOWTs) are easy to implement in deep water farms and are likely to develop strongly in the coming years. This type of wind turbine is gigantic in size (with height of almost 100 m and 150 m with the blades), very heavy (with a mass of almost 1000 tons) and has dynamic characteristics that are difficult to control. Most wind turbine primary resonances are below 1 Hz (typically 0.3 Hz to 0.5 Hz) and possess very small intrinsic damping. FOWTs are subjected to different types of dynamic loads such as environmental loads (wave and wind), aero-structure interaction loads and mechanical loads (inertial and controller effects). These loads induce vibrations in the wind turbine mast that are transmitted in the floating foundation and mooring lines, increasing the overall ultimate loads and fatigue cycling.

Mitigating the vibration of wind turbines (WTs) under dynamic loading such as wind, sea waves, earthquakes has been addressed by many researchers (see Zuo, Bi, et al. 2020). As no external energy is needed, most studies had been conducted on passive linear device, such as single (TMDs) or multiple tuned mass dampers (MTMDs) or tuned liquid dampers (TLDs) thanks to their ability to enhance the damping of the whole system. Classically, a TMD is optimized in the vicinity of a particular frequency of the WT to be controlled and is effective in a narrow frequency band. Slight frequency detuning between the TMD and structure to be controlled may significantly alter the efficiency of the TMD. FOWTs are often located in harsh marine environments and their natural resonances are altered not only by discrepancies between design and construction but also by operational conditions, material property degradation or structural damage.

Since the first seminal work by Gendelman, Manevitch, et al. (2001) twenty years ago, the nonlinear passive dynamical absorber (also known as the nonlinear energy sink - NES), that can be viewed as an extension of the Den Hartog's TMD correcting its lack of robustness to a variation of the primary system, has received an increasing attention by the community and industrial (Ding et al. 2020). NES is usually made of a small mass, a viscous damper and a pure nonlinear stiffness element. The essentially nonlinear stiffness enables a system dynamics without a fixed frequency, leading to a large frequency band ability in dissipating energy from the host structure. Therefore, NESs are robust against any structural frequency changes. As shown by Gendelman, Manevitch, et al. (2001), a restoring force of a third-order power of deformation results in a vibrational energy of the controlled structure to be transferred to cubic NES irreversibly. Since then, many kind of NESs had been designed, such as serial cubic NESs (Gendelman, Sapsis, et al. 2011), bi-stable NESs (AL-Shudeifat 2014), magnet-based NESs (Chen et al. 2020), vibro-impact NESs (Gourc et al. 2015) or track-NESs providing non-linear restoring force similar to that of a cubic-like NES (Wang et al. 2015) in order to improve their efficiency. A particular Track-NESs, providing a non-linear restoring force similar to that of a bistable-like NES has been recently used by Zuo and Zhu (2022) to control earthquake-induced vibration in OWTs.

One of the main difficulty occurring when a NES is used to mitigate vibration motion is that, under periodic forcing, there exists high amplitude detached resonance solution in frequency responses curves of oscillating systems with non linearity, that which must absolutely be avoided. The occurrence of such detached resonances in nonlinear oscillators is known since a long time ago (Rauscher 1938; Abramson 1955). The non linearity could be that of the elastic restoring force as shown, for example, by Alexander et al. (2009) or that of the damping force as shown by Habib, Cyrillo, et al. (2018). To overcome this difficulty, the parameters of the NES must be limited in a particular region of space parameter as shown in Gourc et al. (2014). While efficient, this procedure limits the possibility of maximize the attenuation obtained by the NES.

The most interesting way to overcome such detached resonance is the use of tuned nonlinear damping. As shown by Starosvetsky et al. (2009) who use a quadratic damping which characteristics are composed of two parts: a low and a high amplitude quadratic dampings that differ only by their coefficient: the damping force $f = \lambda_1 \dot{x}|\dot{x}|, x < x_{cr}$ and $f = \lambda_2 \dot{x}|\dot{x}|, x > x_{cr}$. By using the Manevitch's complexification-averaging under 1:1 resonance, the authors compute the slow invariant manifold (SIM) of the system that allows to analyze the strongly modulated response (SMR), which is the best way yo dissipated energy in such system; they observe that the destruction of the detached resonance is achieved when the high amplitude quadratic damping coefficient λ_2 is sufficiently greater than λ_1, they gave a ratio of 12 in their example. The problem indicated by the authors is that the optimization procedure fails when the upper detached resonance merge with the lower branch main resonance curve. It is worth noting that the main resonance curve can be viewed as the frequency response curve (FRF) of the usual linear system. In a similar manner, viscous nonlinear damping had been studied by Andersen et al. (2012) who define a NES constituted by of a mass attached to two additional elements composed of inclined parallel linear spring–damper pairs. The transverse motion of the mass induces not only linear and cubic stiffness (that is the usual way to construct nonlinear spring and NES) but also linear and cubic viscous damping. In their work, the authors had found that, because of the presence of nonlinear damping, the structure can exhibit dynamical instabilities.

This kind of nonlinear damping is analogous as that observed by Bellet et al. (2010) when applying the concept of targeted energy transfer to the field of acoustics using high-amplitude vibrating membrane acting as NES. It was also used by Liu et al. (2019) that generalize the NES by allowing the inclined parallel linear spring–damper pairs to form an initial angle ϕ_0 at rest. This allows not only high amplitude transverse motion but also, depending on the initial angle of inclination, the dynamic of the system can be either hardening or softening at different phases of the motion. In this work the authors observed that using appropriate values for the NES parameter, unwanted detached resonances can be completely eliminated.

The NES model proposed by Andersen et al. (2012) constitutes the basis of the work presented hereafter.

In this paper, only aero-structure interaction loads are considered. FOWTs operate over a wide wind speed range (typically between 5 and 40 knots) and their operating principle is that the blade rotation speed is essentially constant. Practically, as shown by Pahn et al. (2012) in real cases, the mast of a wind turbine is subjected to a thrust forcing composed of an almost constant term and a periodic forcing: $F(t) = A_0 + A\cos(\omega t)$, with $\omega = 2\pi f$, where f is the forcing frequency which mainly depends on the wind speed fluctuations, rotation speed of the FOWT and of blade number. In the various cases considered by the authors, most of the dynamic components is located below 1 Hz with a maximum amplitude of about 10 kN.

To simplify the calculations, the wind turbine is described as a linear mass-spring-damper system coupled to an NES with linear and cubic characteristics for stiffness and damping.

In this paper, we are interested in optimizing the parameters (linear and nonlinear stiffness and nonlinear damping) of the NES for the vibration control of this toy model over its entire operating range under periodic forcing.

To do so, a two passes procedure is proposed. During the first pass, by imposing zero initial condition, one limits the appearance of detached resonance and for a series of fixed NES mass and linear damping, NES linear and nonlinear stiffness are optimized to reduce FOWT vibration over its whole forcing range. Once optimal parameters determined, non-zero initial conditions are imposed to put in evidence detached resonances and nonlinear damping is adjusted to cancel it.

Results obtained over a large domain of parameters suggest that both NES optimal parameter (linear and nonlinear stiffness and nonlinear damping) and attenuation of FOWT vibratory motion depend upon simple power laws of NES mass and linear damping.

This paper is organized as follows. The second section is devoted to the description of the problem. Section three is devoted to the presentation of numeric method that solve the exact equations and to introducing optimization under two aspects, the first by using literature results that avoid detached resonance problem and the second one, by showing how the very good optimization obtained by using brute force without accounting detached resonance is completely wiped out when they appear. The fourth section is devoted to an analytical study of the non linear damping to show that when it is used to control detached resonance, is does not modify the underlying mechanism of energy transfer. Cancellation of detached resonance is studied analytically under 1:1 resonance. It is shown that the NES with a properly tuned nonlinear viscous damping allow the complete elimination of undesired regimes and completely restores the absorber ability to strongly limit floating offshore wind turbine vibration over its whole forcing range. To be sure that this nonlinear damping does not modify too much the dynamic of the system, the slow flow of the system is studied by computing its slow invariant manifold. It is showed that, while not perfectly describe all the feature of the exact solution, most of the characteristics of the slow flow are conserved when nonlinear damping is accounted for. The fifth section is devoted to a synthetic presentation of optimization results obtained by using brute force and detached resonance cancellation. The sixth section is devoted to the conclusion.

2 Equations of the problem

The wind turbine considered in the present article has a resonance frequency of 0.50 Hz and a damping ζ_0 of 0.05%. The forcing frequency f considered in this paper varies over a third of an octave around 0.50 Hz (in the vicinity of the resonance of the wind turbine) and the force applied to the wind turbine mast A varies between 0 and 10 kN. In the following, the constant term A_0 is neglected.

Let us denote $x(t)$ the displacement of the wind turbine and $q(t)$ that of the NES with $w(t) = x(t) - q(t)$. With the classical convention $\dot{x}(t) = \mathrm{d}x(t)/\mathrm{d}t$, the 2 degrees of freedom (2 d-o-f) system is written as

$$m_0\ddot{x}(t) + c_0\dot{x}(t) + k_0x(t) + c_N(1 + 2\nu_N w^2(t))\dot{w}(t) + k_{1N}w(t) + k_{3N}w(t)^3 = A\cos(\omega t) \quad (1)$$

$$m_N\ddot{q}(t) - c_N(1 + 2\nu_N w^2(t))\dot{w}(t) - k_{1N}w(t) - k_{3N}w(t)^3 = 0, \quad (2)$$

where $m_0 = 10^6$ kg is the FOWT weight and $k_0 \approx 10^7$ N/m its stiffness which leads to a pulsation $\omega_0 = \sqrt{10} \approx \pi$. A damping coefficient $\zeta_0 = 0.05\%$ leads to a viscosity $c_0 = 2\zeta_0 m_0 \omega_0 \approx$ 3200 N.s/m. m_N is the NES mass, k_{1N} is the linear stiffness of the NES and k_{3N} its cubic stiffness coefficient. c_N is the coefficient of the linear viscosity of the NES. The nonlinear viscous damping $(1 + 2\nu_N w^2(t))\dot{w}(t)$ which is used is derived from the work of Andersen et al. (2012); $c_N \nu_N$ is the nonlinear viscous damping coefficient.

To these differential equations initial conditions must be imposed: $x(0) = x_0$, $\dot{x}(0) = \dot{x}_0$, $q(0) = q_0$, $\dot{q}(0) = \dot{q}_0$.

Let us define non-dimensional parameters $\Omega = \omega/\omega_0$, $\tau = \omega_0 t$, $\epsilon = m_N/m_0$, $\lambda_0 = c_0/(m_N\omega_0)$, $\lambda_N = c_N/(m_N\omega_0) = \mu_N\lambda_0$, $\delta_N = k_{1N}/(m_N\omega_0^2)$, $K_N = k_{3N}/(m_N\omega_0^2)$ and $F = A/(m_N\omega_0^2)$. The previous system is then written as

$$\ddot{x}(t) + \epsilon\lambda_0\dot{x}(t) + x(t) + \epsilon\mu_N\lambda_0(1 + 2\nu_N w^2(t))\dot{w}(t) + \epsilon\delta_N w(t) + \epsilon K_N w(t)^3 = \epsilon F\cos(\Omega t) \quad (3)$$

$$\epsilon\ddot{q}(t) - \epsilon\mu_N\lambda_0(1 + 2\nu_N w^2(t))\dot{w}(t) - \epsilon\delta_N w(t) - \epsilon K_N w(t)^3 = 0 \quad (4)$$

The solution of this system can be calculated numerically without difficulty. For example, under a laptop workstation, the numerical solution using the NSolve Wolfram Research, Inc. (2021) function takes a fraction of a second for each amplitude-frequency pair for a calculation carried out over a forcing duration of more than an hour.

3 Optimization of the exact equations

3.1 Optimization using rules of the literature

A first optimization, which only takes into account the linear component of the damping, has been carried out using rules from the literature, such as the one proposed for K_N by Starosvetsky et al. (2008). The chosen parameters that avoid the problem of detached resonance by the procedure described in Gourc et al. (2014) have been set as: $\epsilon = 0.01$, $\lambda_0 = 0.1$, $\mu_N = 2$, $\delta_N = 0.03$ and $K_N = 28$. The amplitude-frequency response surface which covers 1/6 of an octave on either side of the resonance of the wind turbine is presented in Figure 1. In this figure $L(A, f) = x_{rms}(A, f)/A$, where $x_{rms}(A, f)$ is the root mean square value of the steady state FOWT amplitude for a given amplitude A and forcing frequency f and $x_{rms}(A, f)$ is estimated by averaging the value of $x(t)$ over the last 1/2h of motion. All calculations made in this study to solve the initial system composed of equations (1) and (2) consider 101 points in frequency and 16 points in amplitude and each of it requires about one minute of total time using parallel computation on 16 cores of a workstation Dell Poweredge R640.

In Figure 1 and all figures herein, all the results about level are given in decibel, calculated as $20\log(|L|/L_r)$, where $L_r = 1$ is the reference level. The left sub-figure in Figure 1 corresponds to the surface response over the whole amplitude and frequency range and the right sub-figure correspond to the ridge curve with free and blocked NES (to see its efficiency). The ridge curve is obtained by taking, for each amplitude, over the frequency range considered, the maximum frequency response; this is mandatory as for such nonlinear system, the frequency of the maximum of the frequency response varies with forcing amplitude; obviously when the NES is blocked, the maximum amplitude is constant. The ridge curve shows a quasi linear decrease in amplitude, this is the usual effect of the NES that acts a amplitude limiter over its efficiency range.

These results are compared with those from an optimized linear absorber (Tuned Mass Damper - TMD), with a mass identical as that of the NES, to control the resonance at 0.5 Hz. Many expressions are available for the parameters (δ_{TMD} characterizes the linear stiffness and μ_{TMD} the linear damping) in the literature since the pioneering work by Den Hartog (1947). We have used those, valid for undamped system as it is almost the case for the FOWT under consideration, proposed by Bakre et al. (2007):

$$\delta_{TMD} = \frac{2+\epsilon}{2(1+\epsilon)^2}, \mu_{TMD} = \frac{1}{\lambda_0}\sqrt{\frac{\epsilon(3\epsilon+4)}{8(1+\epsilon)(2+\epsilon)}}. \quad (5)$$

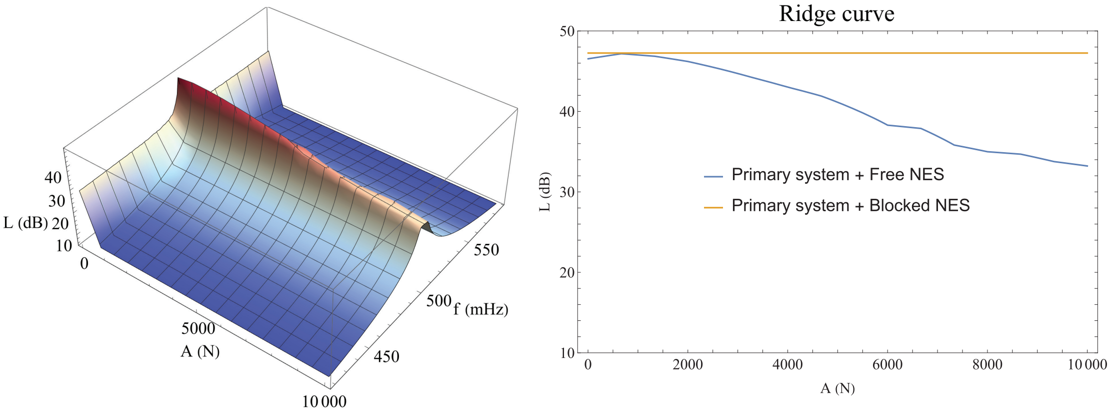

Figure 1: Frequency response of the wind turbine with $f_0^r = 0.5$ Hz with NES. Left: 3D surface response. Right: ridge curve.

The comparison is given in Figure 2. In this figure and the followings, the attenuation is represented as the inverse of the gain $G(A)$ provided by the NES and by a TMD: a negative value of the gain indicates a decrease in vibration level and then an attenuation, while a positive value indicates an increase in vibration level. The various gain curves are simply the ridge curves of the FOWT normalized by its amplitude, in decibels, at its main resonance without accounting for nonlinear components for the NES (*i.e.* a 2 d-o-f linear damped linear system). The TMD characteristics given by equations (5) are, for the FOWT under consideration with $\epsilon = 0.01$, $\delta_{TMD} = 0.985$ and $\mu_{TMD} = 0.498$. For each amplitude A, the level $G(A)$ of the normalized ridge curve is defined by $G(A) = \max_f L(A, f)/(A \max_f L_{\text{lin}}(f))$, where $\max_f L_{\text{lin}}(f)$ is the maximum amplitude of the corresponding linear system, obtained by canceling the non linear part of the NES characteristics in equations (1) and (2). The attenuation allowed by the TMD is calculated in a similar way and remains constant all over the amplitude range.

In the example illustrated in Figure 2, the maximum amplitude of the 2 d-o-f system is reached at the resonance frequency of the FOWT without NES, near 0.5 Hz. However, the resonance frequency of the NES in linear regime is much smaller and lies outside of the plotted range. This resonance frequency is around 0.09 Hz because $\delta_N = 0.03$ implies a linear resonance frequency of $0.5 \times \sqrt{\delta_N} \approx 0.09$ Hz for the NES and lies outside the plotted range.

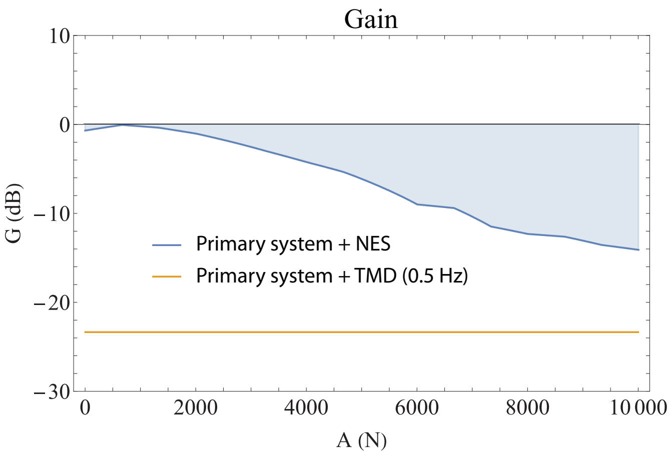

Figure 2: Attenuation (*i.e.* inverse of gain) for NES and TMD optimized for 0.5 Hz resonance

These results are satisfactory, with a maximum reduction in vibration level $20 \log |G|$ of -14 dB and a mean average of -5.3 dB. The objective of the optimization in the next sections is to achieve a higher attenuation. As for the present configuration, the TMD allows a much better reduction of 23.3 dB, we wanted to get as close as possible of the TMD result.

3.2 Optimization using brute force: problem of detached resonances

Among the possible choices of functional, we chose to minimize the ridge curve $G(A)$ mean average in order to obtain the highest mean average attenuation. It corresponds to the shaded area presented in Figure 2. At this stage, in order to avoid, if possible, detached resonances, for each calculation the initial conditions are set to zero: $x_0 = 0$, $\dot{x}_0 = 0$, $q_0 = 0$ and $\dot{q}_0 = 0$.

Minimizing only for the highest forcing excitation, $A_{max} = 10000$ N in the present study, would have been too irrelevant since, in many cases, detached resonances appear around A_{max} even for zero initial conditions and transform the minimization process into a non-convergent process.

Then the functional J to be minimized is defined as

$$J = \frac{1}{A_{max}} \int_0^{A_{max}} G(A)\mathrm{d}A \tag{6}$$

Without constraints on the parameters (ϵ, μ_N, δ_N, K_N) all optimizations led to systematically increase the mass of the NES ϵ and to reduce its damping μ_N. The solution is to fix the pair of parameters ϵ and μ_N and to optimize for each pair δ_n and K_N. The optimization, for two parameters, under Mathematica (Wolfram Research, Inc. 2021) uses a Nelder-Mead type algorithm and requires between 2 and 3 days of parallel computation using 16 cores on a workstation Dell Poweredge R640.

For example, let us take $\epsilon = 0.02$ and $\mu_N = 0.2$, we obtained the optimal parameters $\delta_n = 0.5$ and $K_N = 43$ with an average attenuation $20 \log |J|$ of -16.1 dB and a maximum attenuation achieved at $A = A_{max}$ $G(A_{max}) = -28.1$ dB, to be compared with the -31 dB attenuation provided by the TMD observed in the Figure 3, the TMD characteristics given by equations (5) are for this case $\delta_{TMD} = 0.97$ and $\mu_{TMD} = 1.4$. We note that we recover a classic result from the literature (Habib and Romeo 2020) for which, albeit resorting to different mechanical properties, the TMD and the NES have similar performance when the NES is optimized for a given forcing.

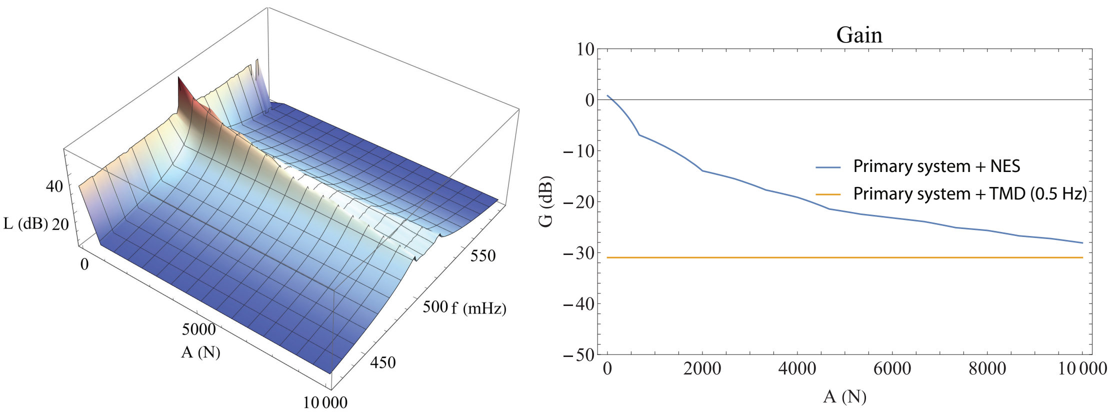

Figure 3: Optimal attenuation for $\epsilon = 0.02$ and $\mu_N = 0.2$

Naturally, when the possibility of one or more detached resonances is taken into account by imposing non zero initial conditions: $x_0 = 0.1$, $\dot{x}_0 = 0.1$, $q_0 = 0$ and $\dot{q}_0 = 0$, the results change completely as shown in Figure 4. These are completely degraded and the NES no longer has any vibration reduction action.

4 Nonlinear damping as a controller of detached resonance: analytical study

Before optimize the non-linear damping parameter ν_N, we have to check that this type of damping does not modify the nature of the solution. To do so, we compute, under the assumption that the motion is under $1:1$ resonance, the fixed points and the Slow Invariant Manifold (SIM) of the system.

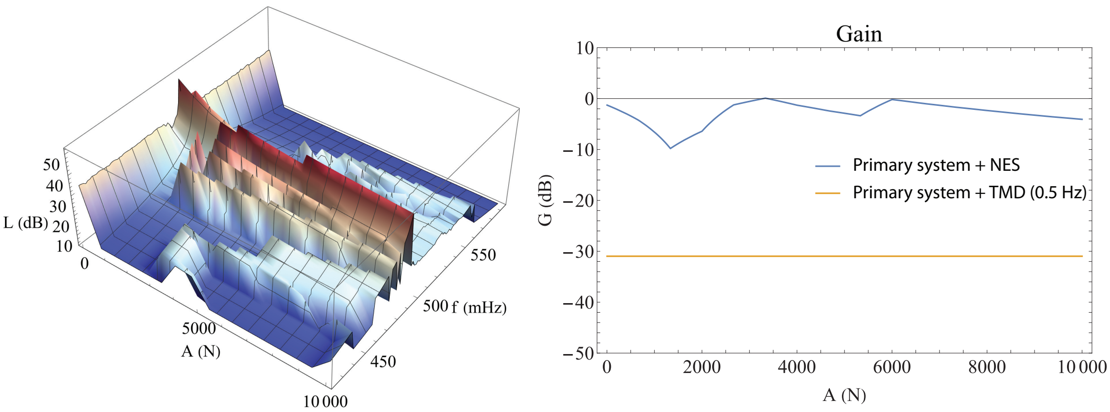

Figure 4: Attenuation for $\epsilon = 0.02$, $\mu_N = 0.2$, $\delta_n = 0.5$ and $K_N = 43$ with detached resonance

4.1 Fixed points

Under $1:1$ resonance, we apply the Manevitch complexification-averaging (CX-A) method. We start from the initial system formed by the equations (3) and (4) in which we perform the change of variable $v = x + \epsilon q$, this leads to

$$\ddot{v} + \frac{v+\epsilon w}{1+\epsilon} + \epsilon\lambda_0 \frac{\dot{v}+\epsilon\dot{w}}{1+\epsilon} = \epsilon F\cos(\Omega t) \quad (7)$$

$$\ddot{w} + \frac{v+\epsilon w}{1+\epsilon} + \epsilon\lambda_0 \frac{\dot{v}+\epsilon\dot{w}}{1+\epsilon} + \delta_N(1+\epsilon)w + \mu_N\lambda_0(1+\epsilon)(1+2\nu_N w^2)\dot{w} + K_N(1+\epsilon)w^3 = \epsilon F\cos(\Omega t) \quad (8)$$

By CX-A, we introduce new variables $\Phi_1\exp(\imath\Omega t) = \dot{v} + \imath\Omega v$ and $\Phi_2\exp(\imath\Omega t) = \dot{w} + \imath\Omega w$ in the preceding system then by averaging over the frequency Ω and we obtain the system of equations

$$\dot{\Phi}_1 + \imath\frac{\Omega}{2}\Phi_1 + \frac{1}{2(1+\epsilon)}\left(\epsilon\lambda_0 - \frac{\imath}{\Omega}\right)(\Phi_1+\epsilon\Phi_2) = \epsilon\frac{F}{2} \quad (9)$$

$$\dot{\Phi}_2 + \imath\frac{\Omega}{2}\Phi_2 + \frac{1}{2(1+\epsilon)}\left(\epsilon\lambda_0 - \frac{\imath}{\Omega}\right)(\Phi_1+\epsilon\Phi_2) - \imath\delta_N\frac{(1+\epsilon)}{2\Omega}\Phi_2 + \mu_N\lambda_0\frac{(1+\epsilon)}{2}\Phi_2 - \frac{3\imath K_N'}{8\Omega^3}(1+\epsilon)|\Phi_2|^2\Phi_2 = \epsilon\frac{F}{2} \quad (10)$$

with $K_N' = K_N\left(1 - \nu_N\mu_N\lambda_0\frac{2\Omega}{3\imath K_N}\right)$. It is easy to see that taking into account the non-linear damping leads to a simple modification of the non-linear stiffness term. It is worth noting that this system represents the slow flow of the steady-state dynamics under condition of 1:1 resonance.

The fixed points $\Phi_{1,2}^0$ are solutions of the slow flow for $\dot{\Phi}_{1,2} = 0$. They are given by:

$$\Phi_1^0 = \frac{\imath\epsilon\Phi_2^0 + \epsilon F(1+\epsilon)\Omega - \epsilon^2\lambda_0\Phi_2^0\Omega}{\imath(\Omega^2-1) + \epsilon\Omega(\imath\Omega+\lambda_0)}, \quad (11)$$

$$\Phi_2^0 \text{ solution of equation } 1 + c_1\,\Phi_2^0 + c_2\,\Phi_2^0|\Phi_2^0|^2 = 0, \quad (12)$$

where the coefficient A and B are given by

$$c_1 = \frac{1}{F\epsilon\Omega^3}\left(-\imath\delta_N + \lambda_0\Omega\left(\mu_N + \epsilon\delta_N\right) + \imath\Omega^2\left(1 + (1+\epsilon)\delta_N - \epsilon\lambda_0^2\mu_N\right) - \lambda_0\Omega^3\left(\epsilon + (1+\epsilon)\mu_N\right) - \imath\Omega^4\right), \quad (13)$$

$$c_2 = \frac{3K_N'\left(-\imath + \epsilon\lambda_0\Omega + \imath(1+\epsilon)\Omega^2\right)}{4\epsilon F\Omega^5}. \quad (14)$$

To be solved, Equation (12) is transformed into a polynomial in $|\Phi_2^0|$ as

$$1 + a_1|\Phi_2^0|^2 + a_2|\Phi_2^0|^4 + a_3|\Phi_2^0|^6 = 0, \quad (15)$$

where the real coefficients of this polynomial are given by

$$a_1 = -|c_1|^2, \quad (16)$$
$$a_2 = -|c_1 + c_2|^2 + |c_1|^2 + |c_2|^2, \quad (17)$$
$$a_3 = -|c_2|^2. \quad (18)$$

The polynomial of degree 3 in $|\Phi_2^0|^2$ given in Equation (12) possesses one or three real roots that depend on the system parameters. Stability of these roots is obtained by an usual linearisation of a complex perturbation around the fixed points. Roughly, it consists in adding small perturbation around fixed points

$$\Phi_1 = \Phi_1^0 + \rho_1, \quad (19)$$
$$\Phi_2 = \Phi_2^0 + \rho_2. \quad (20)$$

The change of variables given in Equations (19) and (20) is introduced in the averaged system composed by Equations (9) and (10). After linearisation, one is left with the following system

$$\begin{pmatrix} \dot\rho_1 \\ \dot\rho_2 \\ \dot\rho_1^\star \\ \dot\rho_2^\star \end{pmatrix} = \begin{pmatrix} A_{11} & A_{12} & 0 & 0 \\ A_{21} & A_{22} & 0 & A_{24} \\ 0 & 0 & A_{11}^\star & A_{12}^\star \\ 0 & A_{24}^\star & A_{21}^\star & A_{22}^\star \end{pmatrix} \begin{pmatrix} \rho_1 \\ \rho_2 \\ \rho_1^\star \\ \rho_2^\star \end{pmatrix} \quad (21)$$

where the $z^\star$ denotes the complex conjugate of z. The coefficients of the matrix are given by:

$$A_{11} = -\imath\frac{\Omega}{2} - \frac{1}{2(1+\epsilon)}\left(\epsilon\lambda_0 - \frac{\imath}{\Omega}\right) \quad (22)$$
$$A_{12} = \epsilon A_{21} \quad (23)$$
$$A_{21} = -\frac{1}{2(1+\epsilon)}\left(\epsilon\lambda_0 - \frac{\imath}{\Omega}\right) \quad (24)$$
$$A_{22} = -\imath\frac{\Omega}{2} - \frac{\epsilon}{2(1+\epsilon)}\left(\epsilon\lambda_0 - \frac{\imath}{\Omega}\right) + \imath\delta_N\frac{(1+\epsilon)}{2\Omega} - \mu_N\lambda_0\frac{(1+\epsilon)}{2} + \frac{3\imath K_N'}{4\Omega^3}(1+\epsilon)|\Phi_2|^2 \quad (25)$$
$$A_{24} = +\frac{3\imath K_N'}{8\Omega^3}(1+\epsilon)\Phi_2^2 \quad (26)$$

Stability of the fixed points is determined for calculating roots of the characteristic polynomial of the matrix of the system given in Equation (21). If all the roots possess a negative real part, then the fixed point is stable. If a real root crosses the half complex plane, the fixed point is saddle-node. If a pair of complex roots leaves the left part of the complex plane, there is a slow flow Hopf bifurcation.

Once amplitude $|\Phi_2^0|$ calculated, by writing $\Phi_2^0 = |\Phi_2^0|\exp(\imath\theta)$, it is easy to show that the phase θ is given by $\theta = \pi - \imath\ln(c_1|\Phi_2^0| + c_2|\Phi_2^0|^3)$. Then Φ_1^0 is calculated by solving Equation (11) for each value of Φ_2^0.

By introducing a detuning parameter σ such as $\Omega = 1+\epsilon\sigma$, we obtain for $A = 10\,000$ N, $\epsilon = 0.02$, $\mu_N = 0.2$, $\delta_N = 0.5$ and $K_N = 43$ the stable fixed points of the primary system displacement normalized by the forcing $|x^0|/F$, where it is recalled that $F = A/(m_N\omega_0^2)$, with and without nonlinear damping which are presented in Figure 5: $|x^0|/F = \left|(\Phi_1^0 + \epsilon\Phi_2^0)/(1+\epsilon)^2\right|/F$. In this figure, the center frequency, obtained for $\sigma = 0$ is $f_0 = \frac{\omega_0}{2\pi}\sqrt{\left(1 + \delta_N(1+\epsilon) + \sqrt{1 + \delta_N(1+\epsilon) - 4\delta_N}\right)/2} \approx 0.51$ Hz corresponds to the highest frequency of the 2 d-o-f linear system without damping. The minimum frequency corresponding to $\sigma \approx -16$ is $f_{min} \approx 0.34$ Hz and the maximum frequency corresponding to $\sigma \approx +18$ is $f_{max} \approx 0.68$ Hz. In this figure, the gray curve corresponds to the primary system with NES without any nonlinear element, the blue curve is obtained for a nonlinear damping $\nu_N = 0$, showing a high amplitude spurious resonance below natural resonance of the primary system and a small detached resonance curve above natural resonance of the primary system. For intermediate values of the nonlinear damping, the continuous secondary low frequency high amplitude resonance curve splits into two stable branches, one at low frequency with low amplitude and one with high frequency and amplitude, this last one is that to be avoided. The green curve, obtained for a nonlinear damping $\nu_N = 800$ is an example of this splitting of detached resonance. In this case, a small detached resonance zone subsists around $\sigma = -1$ and the chosen nonlinear damping does not suffices to ensure a full control of the high amplitude detached resonance. The red curve is obtained for a nonlinear damping $\nu_N = 922$, the smallest value that cancels the high amplitude detached resonance curve.

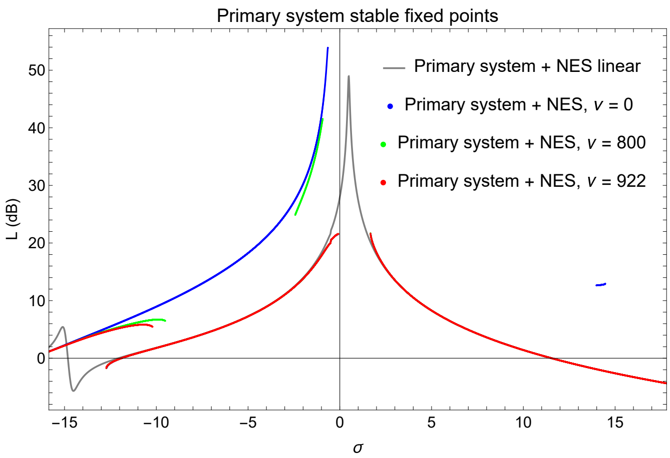

Figure 5: Stable fixed points for $A = 10\ 000$ N, $\epsilon = 0.02$, $\mu_N = 0..2$, $\delta_N = 0.5$, $K_N = 43$, when varying ν_N.

It is worth noting that in this example the frequency range around main resonance of the primary system is twice-wider than that used in the optimization process to show influence of the resonance of the NES at low frequency and high frequency detached resonance. From a practical point of view, it suffices to consider a 1/3 octave total frequency range to estimate the nonlinear damping necessary to cancel the detached resonance.

The fixed points on the main curve (here in red) around the main resonance of the primary system are identical whether linear damping is taken into account or not (the main resonance curves are merged). On the other hand, introducing the non-linear damping prevents the detached resonance without modifying the solution around the resonance of the linear system to be controlled; in the present example, and also in all the examples tested, there is only a very slight difference in the calculated level (less than 1 dB) with anD without nonlinear damping at the boundaries of the stable zone near the main resonance of the primary system, around $\sigma = 0$ and $\sigma = 2$ in Figure 5.

4.2 Slow invariant manifold

A very efficient way to attenuate the vibration is observed under Strongly Modulated Response (SMR) in the vicinity of the $1:1$ resonance. Two time scales $\tau_0 = t$ and $\tau_1 = \epsilon t$ appear naturally in this type of motion and a multi-scale asymptotic development to order 0 in ϵ allows us to obtain this manifold. Let us state $\Phi_i = \phi_i^0 + \epsilon\phi_i^1 + O(\epsilon^2)$, we obtain to the order 0 in ϵ the following set of differential equations:

$$\dot{\phi}_1^0 = 0 \tag{27}$$

$$\dot{\phi}_2^0 + \frac{\imath}{2}\left(\phi_2^0 - \phi_1^0\right) - \frac{\mu_N\lambda_0}{2}\phi_2^0 - \frac{3\imath\tilde{K}'_N}{8}|\phi_2|^2\phi_2 - \imath\frac{\delta_N}{2}\phi_2^0 = 0, \tag{28}$$

with $\tilde{K}'_N = K_N\left(1 - \nu_N\mu_N\lambda_0\frac{2}{3\imath K_N}\right)$. Equation (27) gives $\phi_1^0 = \phi_1^0(t_1, t_2, \cdots) = \phi_1$. The fixed point $\phi_2^0 = \phi_2$ of Equation (28) is solution of

$$\imath\left(\phi_2 - \phi_1\right) + \mu_N\lambda_0\phi_2 - \frac{3\imath\tilde{K}'_N}{4}|\phi_2|^2\phi_2 - \imath\delta_N\phi_2 = 0. \tag{29}$$

Let us write the fixed points under polar form $\phi_1 = \sqrt{Z_1}\exp(\imath\theta_1)$ and $\phi_2 = \sqrt{Z_2}\exp(\imath\theta_2)$. A few algebraic manipulations give the Slow Invariant Manifold (SIM) for $1:1$ resonance capture:

$$Z_1 = \alpha_1 Z_2 + 2\alpha_2 Z_2^2 + 3\alpha_3 Z_2^3, \tag{30}$$

where the real coefficients α_i, $i = 1, 2, 3$ are given by:

$$\alpha_1 = (\delta_N - 1)^2 + \lambda_0^2 \mu_N^2, \tag{31}$$

$$\alpha_2 = \frac{3}{2} K_N (\delta_N - 1) + \nu_N \lambda_0^2 \mu_N^2, \tag{32}$$

$$\alpha_3 = \frac{1}{16}\left(9K_N^2 + 4\nu_N^2 \lambda_0^2 \mu_N^2\right). \tag{33}$$

This SIM has one or three solutions. The bifurcation points are obtained by canceling the derivative of the second member of the equation (30) with respect to Z_2: $\alpha_1 + 2\alpha_2 Z_2 + 3\alpha_3 Z_2^2 = 0$. The two roots of this equation are :

$$Z_2^{(1,2)} = \frac{-\alpha 2 \pm \sqrt{\Delta}}{\alpha_1}, \tag{34}$$

with $\Delta = \alpha_2^2 - 3\alpha_1\alpha_3$, one obtains:

$$\Delta = \frac{1}{4}\left[\left(3K_N(\delta_N - 1) - 2\nu_N \lambda_0^2 \mu_N^2\right)^2 - \frac{3}{4}(1 + \lambda_0^2 \mu_N^2 - 2\delta_N + \delta_N^2)(9K_N^2 + 4\nu_N^2 \lambda_0^2 \mu_N^2)\right]. \tag{35}$$

For $Z_2^{(1,2)}$ to exist, Δ must be positive. It is easy to see form Equation (35) that Δ is a polynomial of degree 2 in δ_N. Let us calculate the values $\delta_N^{(1,2)}$ that cancel Δ. One obtains:

$$\delta_N^{(1)} = 1 + \sqrt{3}\lambda_0 \mu_N \left(\frac{1}{3} - \frac{4}{3 + 2\sqrt{3}\nu_N \lambda_0 \mu_N / K_N}\right) \tag{36}$$

$$\delta_N^{(2)} = 1 - \sqrt{3}\lambda_0 \mu_N \left(\frac{1}{3} - \frac{4}{3 - 2\sqrt{3}\nu_N \lambda_0 \mu_N / K_N}\right) \tag{37}$$

Depending on the value of ν_N, two cases can be considered.

1. if $\nu_N = 0$ and $\sqrt{3}\lambda_0\mu_N < 1$,

$$\delta_N^{(1)} = 1 - \sqrt{3}\lambda_0 \mu_N \tag{38}$$

$$\delta_N^{(2)} = 1 + \sqrt{3}\lambda_0 \mu_N \tag{39}$$

   one can show that $\Delta \le 0$ for $\delta_N \in [\delta_N^{(1)}, \delta_N^{(2)}]$. Then, for Δ to be positive, one must impose $\delta_N \le \delta_N^{(1)}$ or $\delta_N \ge \delta_N^{(2)}$. To ensure that $Z_2^{(1,2)} \ge 0$, it is easy to see from Equation (34), that α_2 must be negative and then, from Equation (32), δ_N can not be greater than 1. Then, one obtains the classical condition (Wu et al. 2021) that when the NES possesses a linear stiffness δ_N, it must satisfy $\delta_N < 1 - \sqrt{3}\lambda_0\mu_N$.

2. if $\nu_N \neq 0$, the procedure differs a little. It is worth noting that, depending on the parameters, $\delta_N^{(1)}$ is not always smaller than $\delta_N^{(2)}$. Let us denote $\nu_N^{\delta} = \frac{\sqrt{3}K_N}{2\lambda_0\mu_N}$, the value of nonlinear damping that makes $\delta_N^{(2)}$ singular. Different sub-cases are to be considered.
   (a) If $\nu_N < \nu_N^{\delta}$, one can show that $\Delta \le 0$ for δ_N lying in the interval limited by $\delta_N^{(1)}$ and $\delta_N^{(2)}$. In the vicinity of ν_N^{δ}, let us consider $\nu_N = \nu_N^{\delta}(1 - \eta)$, $\eta \ll 1$, one has

$$\delta_N^{(1)} \approx 1 - \frac{1}{\sqrt{3}}\lambda_0 \mu_N (1 + \eta) \longrightarrow 1 - \frac{1}{\sqrt{3}}\lambda_0 \mu_N \text{ for } \eta \longrightarrow 0, \tag{40}$$

$$\delta_N^{(2)} \approx 1 + \frac{4}{\sqrt{3}\eta}\lambda_0 \mu_N \longrightarrow \infty \text{ for } \eta \longrightarrow 0. \tag{41}$$

   Then, if $\lambda_0\mu_N/\sqrt{3} < 1$, we must impose that $\delta_N < \delta_N^{(1)}$ and with $\Delta > 0$ close to zero, to ensure that α_2 must be negative, from Equation (32) one has to impose

$\frac{3}{2}K_N(\delta_N-1)+\nu_N^\delta(1-\eta)\lambda_0^2\mu_N^2+O(\eta^2)<0$, then one obtains $\delta_N<1+\frac{1}{\sqrt{3}}\lambda_0\mu_N+O(\eta)$. This condition, together with $\delta_N<\delta_N^{(1)}$, gives that δ_N must satisfies $\delta_N<1-\frac{1}{\sqrt{3}}\lambda_0\mu_N$. Care must be taken when $\nu_N<\nu_N^\delta$ because when $\nu_N\to 0$, condition reads $\delta_N<1-\sqrt{3}\lambda_0\mu_N$ which can significantly differs from the condition $\delta_N<1-\frac{1}{\sqrt{3}}\lambda_0\mu_N$ if $\mu_N\lambda_0$ is not small.

(b) if $\nu_N>\nu_N^\delta$, one can show that $\Delta\geq 0$ for δ_N lying in the interval limited by $\delta_N^{(1)}$ and $\delta_N^{(2)}$. In the vicinity of ν_N^δ, let us consider $\nu_N=\nu_N^\delta(1+\eta)$, $\eta\ll 1$, one has

$$\delta_N^{(1)} \approx 1-\frac{1}{\sqrt{3}}\lambda_0\mu_N(1-\eta)\longrightarrow 1-\frac{1}{\sqrt{3}}\lambda_0\mu_N \text{ for } \eta\to 0, \tag{42}$$

$$\delta_N^{(2)} \approx 1-\frac{4}{\sqrt{3}\eta}\lambda_0\mu_N\longrightarrow -\infty \text{ for } \eta\to 0. \tag{43}$$

Here again, if $\lambda_0\mu_N/\sqrt{3}<1$, we must impose that $\delta_N<\delta_N^{(1)}$ and with $\Delta>0$ close to zero, to ensure that α_2 must be negative, from Equation (32) one has to impose $\frac{3}{2}K_N(\delta_N-1)+\nu_N^\delta(1-\eta)\lambda_0^2\mu_N^2+O(\eta)<0$, then one obtains $\delta_N<1+\frac{1}{\sqrt{3}}\lambda_0\mu_N+O(\eta)$. One finally obtains that δ_N must satisfies $\delta_N<1-\frac{1}{\sqrt{3}}\lambda_0\mu_N$. For the general case $\nu_N>\nu_N^\delta$, no simple rule is available. As a simple rule of the thumb, for ν_N not too large, choose at first approach $\delta_N<1-\frac{1}{\sqrt{3}}\lambda_0\mu_N$, then the criteria detailed above allow us to specify the theoretical limits, keeping in mind that this is an approximate resolution and therefore the effective solutions may differ, especially near the limiting cases $\nu_N\ll\nu_N^\delta$ or $\nu_N\gg\nu_N^\delta$.

The stability of the SIM is obtained by an usual linearisation of a complex perturbation around the fixed points of the system composed by Equation (27) and Equation (28). Without giving too much details, this leads to compute the roots of a third order characteristic polynomial given in Equation (44)

$$\begin{aligned} p(X) &= X^3+\mu_N\lambda_0X^2(1-Z_2^2\delta_N) \\ &-\frac{X}{64}(((-4+3Z_2^2K_N+4\delta_N)(-4+9Z_2^2K_N+4\delta_N)+4\mu_N^2\lambda_0^2(4+Z_2^2\nu_N(-8+3Z_2^2\nu_N))). \end{aligned} \tag{44}$$

If all roots have a real part less or equal to zero, the SIM is stable. The three roots of this polynomials are given by

$$X_1 = 0 \tag{45}$$

$$X_2 = \frac{1}{8}\left(4\mu_N\lambda_0(-1+\nu_NZ_2)+\sqrt{\Delta_X}\right) \tag{46}$$

$$X_3 = \frac{1}{8}\left(4\mu_N\lambda_0(-1+\nu_NZ_2)-\sqrt{\Delta_X}\right) \tag{47}$$

with $\Delta_X=48Z_2K_N(1-\delta_N)-16(1-\delta_N)^2+Z_2^2(-27K_N^2+4\mu_N^2\lambda_0^2\nu_N^2)$. For $Z_2\in]Z_2^{(2)},Z_2^{(1)}[$, the SIM is always unstable. For $\nu_N\gg 1$, as in the general case $Z_2\ll 1$, one has $\Delta_X<0$ and one can approximate the real part of the roots X_2 and X_3 by $\mu_N\lambda_0(-1+\nu_NZ_2)/2$. Then, the SIM is unstable for $Z_2>Z_2^\nu=1/\nu_N$.

An interesting feature of the dependence of the SIM with respect to the nonlinear damping is that it can be shown that $\alpha_1Z_2^{(1)}+2\alpha_2\left(Z_2^{(1)}\right)^2+3\alpha_3\left(Z_2^{(1)}\right)^3=0$ for $\nu_N^0=3/2K_N/(1-\delta_N)$. For example, let us consider $\delta_N=0.5$ and $K_N=43$. One obtains $\nu_n^0=129$. The SIM is plotted in Figure 6 for the parameters $\epsilon=0.02$, $\mu_N=4$, $\delta_N=0.5$ and $K_N=43$ for $\nu_N=0$ and $\nu_N=\nu_N^0$. In this figure, the black dots correspond to the bifurcation points $Z_2^{(1,2)}$; the red dot correspond to Z_2^ν.

This feature of non-linear damping change dramatically the efficiency of the NES. As it is classical that too much damping can destroy SMR, the chosen value $\mu_N=4$ in Figure 6, corresponding to a NES linear damping four times greater than linear system damping (even with

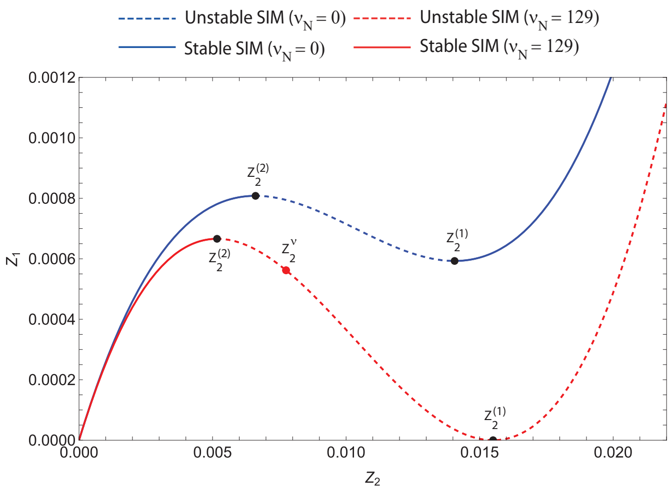

Figure 6: SIM for $\epsilon = 0.02$, $\mu_N = 4$, $\delta_N = 0.5$, $K_N = 43$, $\nu_N = 0$ and $\nu_N = 129$.

such a high value, as $\lambda_0 = 0.1$, the strongest condition $\sqrt{3}\lambda_0\mu_N < 1$ is satisfied), allows a very short range of possible SMR when $\nu_N = 0$ while remaining maximum for $\nu_N = \nu_N^0$. As ν_N^0 does not depends on ϵ nor ν_N, it can not be used as a guide to choose the nonlinear damping that cancels detached resonance for a given ϵ and ν_N.

For the parameters $\epsilon = 0.02$, $\mu_N = 0.2$, $\delta_N = 0.5$ and $K_N = 43$, the value of nonlinear damping that destroy detached resonance for the maximum system forcing amplitude $A = 10000$ N is $\nu_N = 922$. It is worth noting that it suffices to cancel the detached resonance for the highest amplitude to ensure that it is canceled for all lesser amplitudes. We plotted the SIM for $\nu_N = 0$ and $\nu_N = 922$ in Figure 7. In this figure, whatever the value of the non-linear damping, relaxation oscillations (indicated by green arrows) are observed for which there is a possibility of SMR. We obtain the limiting values of Z_1 and Z_2 by $Z_1^* \approx 0.0058$ et $Z_2^* \approx 0.02$.

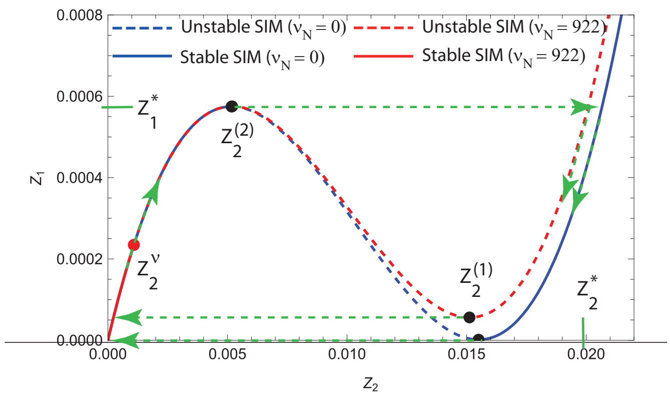

Figure 7: SIM for $\epsilon = 0.02$, $\mu_N = 0.2$, $\delta_N = 0.5$, $K_N = 43$, $\nu_N = 0$ or 922

It is worth noting that in Figure 7, the significant nonlinear damping has modified the shape of the SIM in two ways: first, the bifurcation point $Z_2^{(1)}$ moves away from the abcissa axis, as it is classical for a damped system, for that case $\nu_N^0 = 129$ is far from the necessary nonlinear damping that cancels detached resonance; secondly, and more important, the SIM is stable only for $Z_2 \in [0, 1/\nu_N]$, which correspond only to a small part of of the SIM. In Figure 7, the black dots correspond to the bifurcation points $Z_2^{(1,2)}$ and Z_2^{ν} is indicated as a red dot.

4.3 Numeric simulations compared to the analytical results

The motion resulting from the numerical solution of the problem equations for the parameters : $\epsilon = 0.02$, $\mu_N = 0.2$, $\delta_N = 0.5$, $K_N = 43$, $\nu_N = 822$ and for a forcing $A = 9800$ N, $f = 0.51$ Hz had been plotted in Figure 8. It is worth noting that, in the present case and for all calculations, slightly different values of the nonlinear damping ν_N had been necessary to cancel detached resonance for numerical and analytical results.

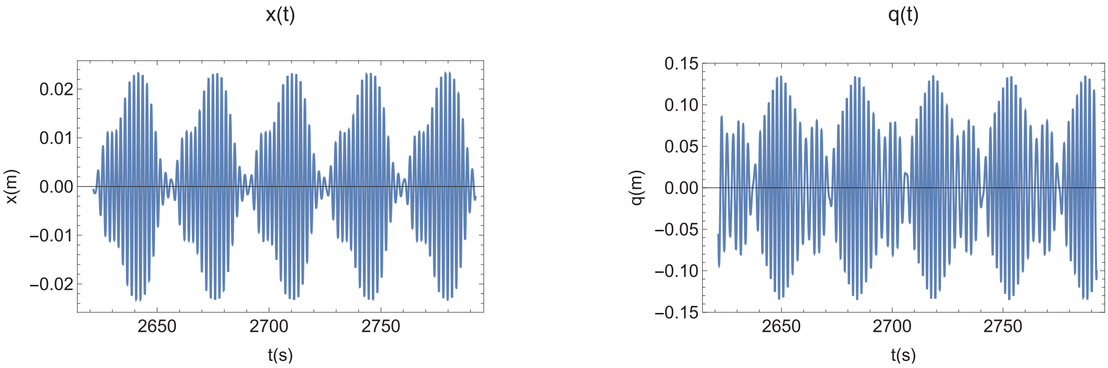

Figure 8: Example of time series $x(t)$ on the left and $q(t)$ on the right under SMR for $A = 9800$ N, $f = 0.51$ Hz, $\epsilon = 0.02$, $\mu_N = 0.2$, $\delta_N = 0.5$, $K_N = 43$ and $\nu_N = 822$

.

We observe that the amplitude maxima correspond to those predicted by the SIM

$$\max x(t) \approx 0.023 \quad \Rightarrow \quad (\max x(t))^2 \approx 0.0053 \approx Z_1^* \tag{48}$$
$$\max q(t) \approx 0.135 \quad \Rightarrow \quad (\max q(t))^2 \approx 0.018 \approx Z_2^*, \tag{49}$$

and that a small plateau for both the primary system $x(t)$, around $x(t) \approx 0.011$, that is $Z_1 \approx 0.00014$, and the NES $q(t)$, around $q(t) \approx 0.065$, that is $Z_2 \approx 0.0053$, in the SMR. This correspond to the small plateau observed in Figure 9 roughly around the unstable point in the SIM given by Z_2^v.

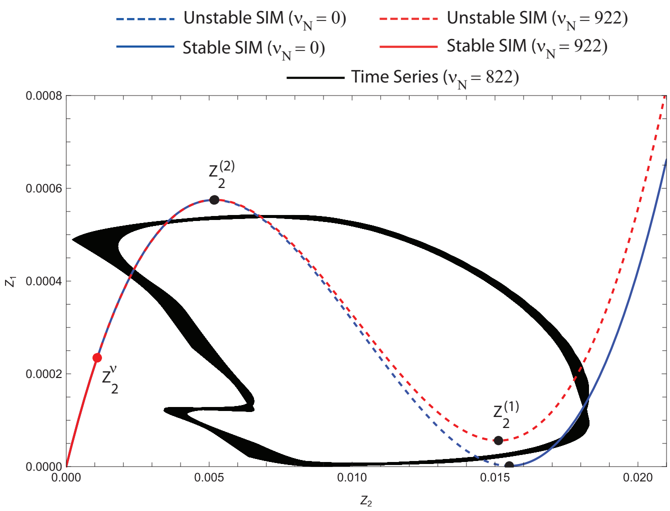

Figure 9: Projection of the time series onto the SIM for $A = 9800$ N, $f = 0.51$ Hz, $\epsilon = 0.02$, $\mu_N = 0.2$, $\delta_N = 0.5$, $K_N = 43$ and $\nu_N = 922$ for analytical calculation or $\nu_N = 822$ for numerical calculation.

While these results seem to be convincing, they must be pondered by the fact that for different forcing conditions, the predictions allowed by SIM under 1:1 resonance are less pertinent. For example, the motion resulting from the numerical solution of the problem equations for the parameters : $\epsilon = 0.02$, $\mu_N = 0.2$, $\delta_N = 0.5$, $K_N = 43$, $\nu_N = 822$ and for a forcing $A = 9000$ N, $f = 0.507$ Hz are plotted in Figure 10.

In the example given in Figure 10, the SMR shows two different shapes. The times series is projected onto the SIM as shown in Figure 11. In this example, the system partially follows the SIM under 1:1 resonance, and it is clear that it jumps regularly onto a different branch of periodic solution.

To have a better understanding of the nature of the transitions that occur, an Hilbert-Huang analysis (see Huang et al. 1998) is conduced on the time series. Without giving too much detail about the Hilbert-Huang transform (HHT), the core of this method is to decompose the signal into what's named empirical modes (so the name empirical mode decomposition - EMD). These

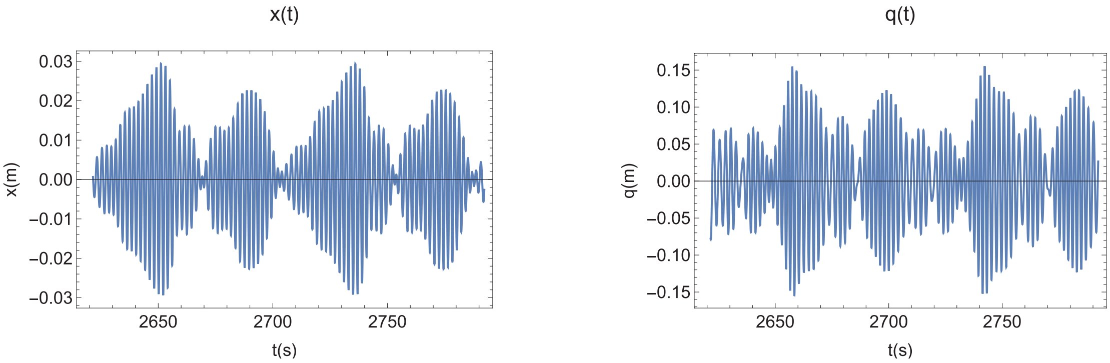

Figure 10: Example of time series $x(t)$ on the left and $q(t)$ on the right under SMR for $A = 9000$ N, $f = 0.507$ Hz, $\epsilon = 0.02$, $\mu_N = 0.2$, $\delta_N =$, $K_N = 43$ and $\nu_N = 922$ for analytical calculation or $\nu_N = 822$ for numerical calculation.

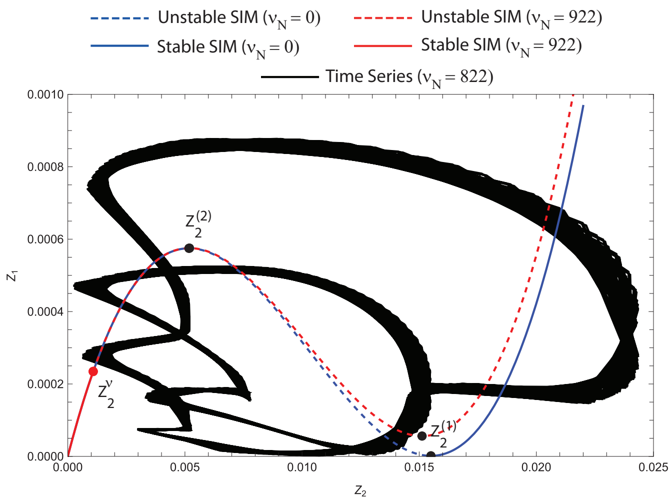

Figure 11: Projection of the time series onto the SIM for $A = 9000$ N, $f = 0.507$ Hz, $\epsilon = 0.02$, $\mu_N = 0.2$, $\delta_N = 0.5$, $K_N = 43$ and $\nu_N = 922$ for analytical calculation or $\nu_N = 822$ for numerical calculation.

based signal modes (the so called intrinsic mode function - IMF) split the signal into decreasing frequency component, each of it possessing by construction only one frequency component at a each time; then a Hilbert spectral analysis - HSA is conduced allowing to compute each IMF's instantaneous frequency. Generally a signal possesses less than 10 IMFs but 20 IMFs is possible on particularly rich signals.

One of the main difficulty of this method is the extraction of the IMFs and the program (a simple executable code working under Windows) proposed by Loudet (2009) allows fast and efficient EMD. For the times series given in Figure 8 and in Figure 10, less than 6 IMFs were necessary to analyze the signals and only the first three contain significant data. The results of HHT analysis of times series presented in Figure 8 is given in Figure 12 for the linear system displacement and in Figure 13 for the NES displacement. The results of HHT analysis of times series presented in Figure 10 is given in Figure 14 for the linear system displacement and Figure 15 for the NES displacement. In each of these figures, three sub-figures are given, the top is the corresponding IMF, the center colored figure is the wavelet analysis of the IMF and the bottom one is the instantaneous frequency obtained by HSA. It is worth noting that the instantaneous frequency curves have been plotted with the convention that the higher the IMF amplitude the darker the curve.

For the regular SMR, corresponding to the time series given in Figure 8, the HHT of the linear system given in Figure 8 reveals that the motion during SMR occurs at the forcing frequency and no significant energy conversion is observed; the first IMF contains most of the energy of the linear system motion. At the transition between two bursts, the motion occurs at small amplitude (amplitude of IMF2 is more or less a hundred less than that of IMF) and has a frequency mainly $f_0/3$ and with an even smaller component on IMF 3 (one third of IMF 2) with a frequency

$f_0/5$. HHT of the NES Motion given in Figure 10, reveals similar comportment with obviously a significant frequency variation fo the NES and amplitude of the second IMF only ten times smaller than the first one with a frequency mainly at $f_0/3$. This indicate a 1:1 resonance capture during the SMR and a 1:3 resonance capture during transition between the two bursts.

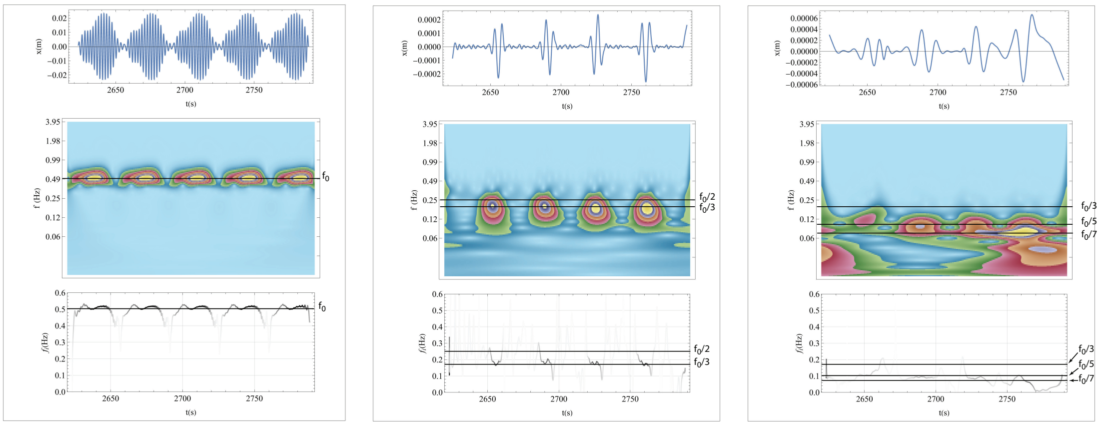

Figure 12: $x(t)$ first (left), second (middle) and third (left) IMF. A = 9800 N, f = 0.51 Hz, ϵ = 0.02, μ_N = 0.2, δ_N = 0.5, K_N = 43 and ν_Φ = 822. Top: IMF, center: Wavelet analysis, bottom: instantaneous frequency.

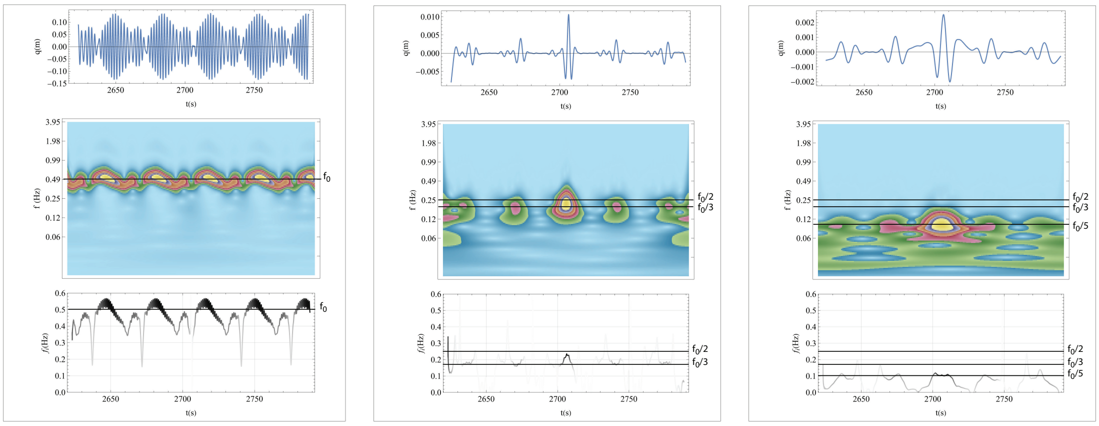

Figure 13: $q(t)$ first (left), second (middle) and third (left) IMF. A = 9800 N, f = 0.51 Hz, ϵ = 0.02, μ_N = 0.2, δ_N = 0.5, K_N = 43 and ν_Φ = 822. Top: IMF, center: Wavelet analysis, bottom: instantaneous frequency.

For the double SMR, corresponding to the time series given in Figure 10, the HHT of the linear system given in Figure 10 reveals that the energy during the two kind of SMR is located at the forcing frequency and no significant energy conversion is observed; the first IMF contains most linear system motion energy. At the transition between two bursts, the motion arose at small amplitude (amplitude of IMF2 is more or less a hundred less than that of IMF) and has a frequency mainly $f_0/3$ and with an even smaller component on IMF 3 (one third of IMF 2) with a frequency $f_0/5$. HHT of the NES motion given in Figure 10, reveals similar comportment with obviously a significant frequency variation for the NES, an amplitude of the second IMF only ten times smaller than the first IMF with a frequency mainly at $f_0/3$. This indicate a 1:1 resonance capture during the SMR and a 1:2 resonance capture for the linear system and a 1:3 resonance capture for the NES during transition between two bursts. This could corresponds to the transient instability leading to 1:3 resonance capture observed by Andersen et al. (2012) with impulse with lower amplitude than that ensuring 1:1 resonance capture at high magnitude impulse. Obviously the systems under study differ by the forcing, impulse for Andersen et al. (2012) and continuous forcing in the present work. But, as noted by Andersen et al. (2012), *this instability is attributed solely to the passive nonlinear damping*. While further analytical studies would had been useful, this is not the core of this work and they are left to future work.

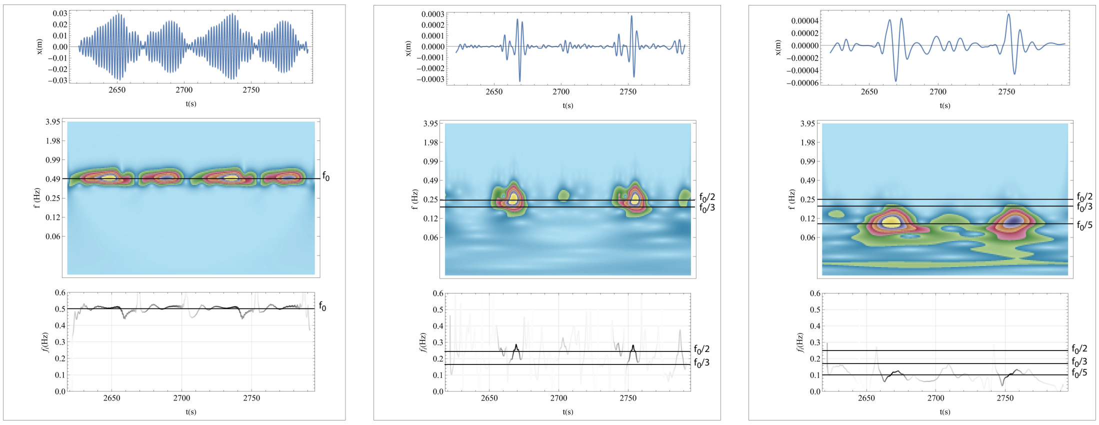

Figure 14: $x(t)$ first (left), second (middle) and third (left) IMF. $A = 9000$ N, $f = 0.507$ Hz, $\epsilon = 0.02$, $\mu_N = 0.2$, $\delta_N = 0.5$, $K_N = 43$ and $\nu_\Phi = 822$. Top: IMF, center: Wavelet analysis, bottom: instantaneous frequency.

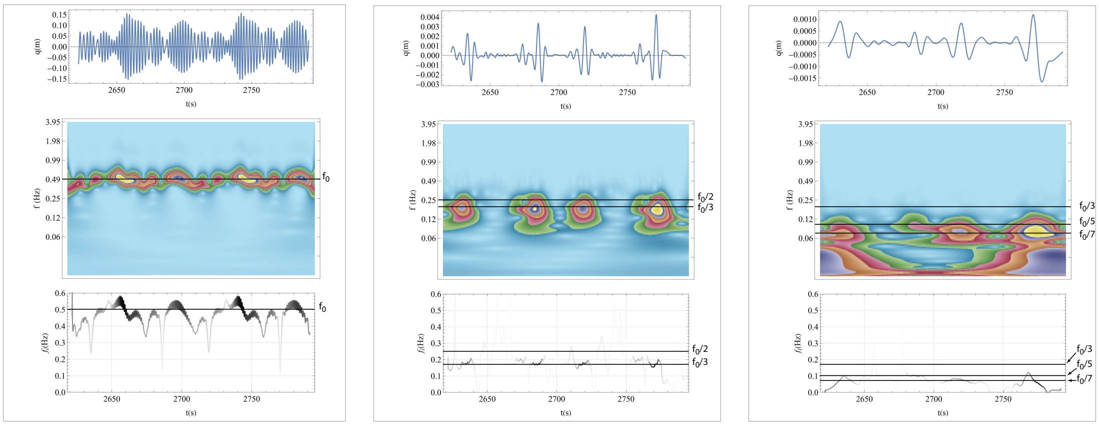

Figure 15: $q(t)$ first (left), second (middle) and third (left) IMF. $A = 9000$ N, $f = 0.507$ Hz, $\epsilon = 0.02$, $\mu_N = 0.2$, $\delta_N = 0.5$, $K_N = 43$ and $\nu_\Phi = 822$. Top: IMF, center: Wavelet analysis, bottom: instantaneous frequency.

All these results clearly show that accounting for nonlinear damping, while modifying the behavior of the system by removing the detached resonances, does not fundamentally alter the nature of the coupling between primary system and NES.

5 Optimization results

We proceeded to the minimization of function J defined in equation (6) of more than a hundred different configurations obtained by fixing ϵ and μ_N for $\epsilon \in [0.001, 0.05]$ and $\mu_N \in [0.1, 1]$ and by looking for the values of δ_N and K_N which allowed the greatest average attenuation over the whole range of forcing of the wind turbine and finally the smallest value of ν_N which avoided the phenomenon of detached resonance.

While not all details are reported here, it is to be noticed that, particularly for small values of ϵ, multiple combinations (2 or 3) of K_N and δ_N lead to comparable values for attenuation. As is in such case it becomes very difficult to estimate an absolute minimum, we decided to choose identified values that ensure, when possible, a regular evolution with respect to the parameters ϵ and μ_N.

An example of multiple minima of J, as defined in equation (6), is given in Figure 16. In this figure, we present a 3D plot and a contour plot of $20 \log |J|$ versus $\delta_N \in [0; 1]$ and $K_N \in [0; 40]$ for $\epsilon = 0.004$ and $\mu_N = 0.3$. In this figure only negative values of J, corresponding to an reduction of vibration of primary system, have been plotted. This shows that two separated minima exist, the first in the vicinity $\delta_N \approx 0.5$, $K_N \approx 5$ and the second in the vicinity of $\delta_N \approx 0.2$, $K_N \approx 8$. A refined study around these two points gives

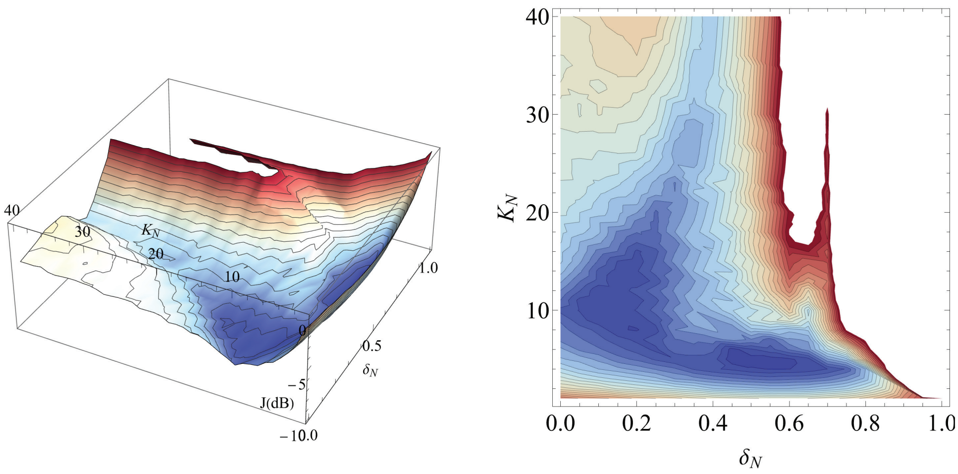

Figure 16: Map of J as a function of δ_N and K_N for $\epsilon = 0.004$ and $\mu_N = 0.3$. Left: 3-D plot, right: contour plot

$$\delta_N = 0.48, K_N = 5.4 \;\Rightarrow\; J = -8 \text{ dB}, \tag{50}$$

$$\delta_N = 0.19, K_N = 8.1 \;\Rightarrow\; J = -7.7 \text{ dB}, \tag{51}$$

while comparable, the first minimum given in (50) gives a slightly better attenuation are a more smooth variation of δ_N nd K_N when ϵ and μ_N vary. It have then be chosen. It is worth noting that for significant range of δ_N and K_N, represented in white in Figure 16, the parameter choice leads to a positive value of J meaning a increase in the response of the linear system that must absolutely avoided. As it has been shown, the linear stiffness must satisfies $\delta_N < 1 - \sqrt{3}\lambda_0\mu_N$, and in the present case, with $\lambda_0 = 0.1$, and $\mu_N = 0.3$, one must have $\delta_N < 0.95$. This limit is observed in the right sub-figure in Figure 16, where whatever K_N, if $\delta_N > 0.95$ then $J > 0$ and the chosen parameters lead to a NES unable in reducing the vibration of the primary linear system.

The results are presented in Figure 17 for δ_N (left sub-figure) and K_N (left sub-figure); in this figure, we presented the parameters δ_N and K_N versus ϵ which give the best attenuation imposing zero initial conditions for different NES linear damping μ_N. It is obvious that for small values of ϵ (say less that 0.5%), both δ_N and K_N show significant variations while becoming more smooth and regular for $\epsilon > 1\%$. For sufficiently high values of ϵ, both parameters show a power dependence with respect to ϵ and μ_N; while not completely clear for δ_N, its obvious for K_N. This will be precised later on.

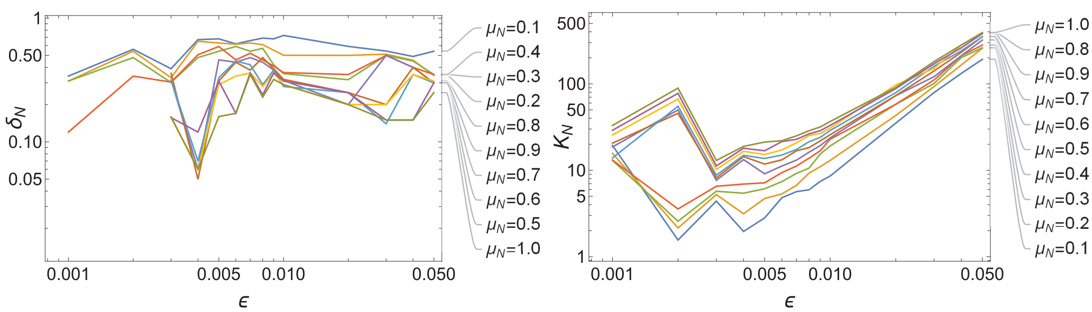

Figure 17: Identified optimal parameter values vs ϵ for different linear damping μ_N. Left: δ_N, right: K_N.

To ensure that solutions will bifurcate onto detached resonance, non zero initial conditions are imposed, and the values of nonlinear damping that cancel it for the highest forcing A_{max} are given in Figure 18. In this figure, the results are presented for analytical approximated solution (left sub-figure) denoted ν_N^a and for numeric simulation of the exact solution (right sub-figure) denoted ν_N^c. Here again, it is clear that for small values of ϵ (say less that 1%), both nonlinear damping obtained from analytical ν_N^a and numeric ν_N^c estimates show significant variations while becoming more smooth and regular for $\epsilon > 1\%$ with comparable numeric values. Without giving too much details, these variations are observed when the function to minimize J possesses more than one minimum and when one of these vanishes or appears when ϵ varies. It is to be remarked that for very low values of ϵ (less that 2%), there is no clear detached resonance and nonlinear damping is useless; but in that case, the NES does not allow an efficient vibration control of the primary linear system (only a few dB) and, combined with high variation in the identification coefficient, the solution with very small ϵ must not be considered as efficient.

As observed for δ_N and K_N, that both parameter ν_N^a and ν_N^c show a power dependence with respect to ϵ and μ_N. For the highest values of ϵ, analytical and computed coefficients of nonlinear damping obtained show significantly high values. However, it must be kept in mind that the damping of the NES is given by $\epsilon\mu_N\lambda_0(1 + 2\nu_N w^2(t))\dot{w}(t)$ with $\lambda_0 = 0.1$ for $\epsilon = 0.01$ and $\mu_N \in [0.1, 1]$. In fact, even if the values of ν_N seem high, the values of $\epsilon\mu_N\lambda_0\nu_N$ remain in acceptable orders of magnitude. To confirm this, let us define a NES mass $m_N = \epsilon m_0 = 10000$ kg and $\mu_N = 0.5$. With $\epsilon = 0.01$, one has $\lambda_0 = c_0/(m_N\omega_0) \approx 0.1$, the optimal values of ν_N is 68 for the numeric computation of the exact equation and 85 for the analytical solution, then we take $\nu_N \approx 80$. For $\mu_N = 0.5$, that is a linear NES damping of half that of the primary system, one has $c_N = 1600$ N.s/m. The non linear damping coefficient is then $2\nu_N c_N \approx 260\,000$ N.s/m, corresponding, for a linear frequency of 0.5 Hz, to an approximate linear damping of $\zeta_N = 2\nu_N c_N/(2m_N\omega_0) \approx 4.$.

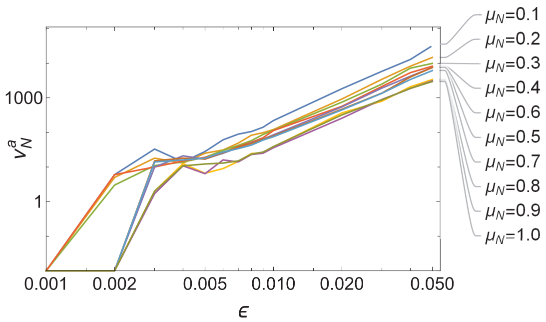

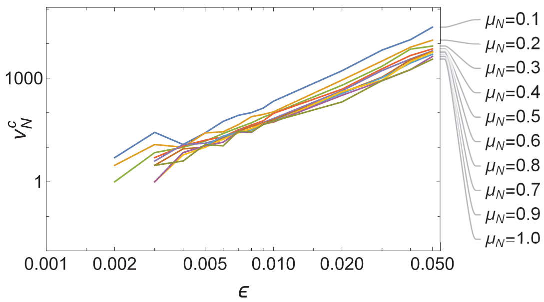

Figure 18: Identified optimal nonlinear damping versus ϵ for different linear damping μ_N. Left: analytical ν_N^a, right: numeric computation ν_N^c.

Finally, we present in Figure 19 the best average gain obtained as a function of the mass ϵ and damping μ_N. In this figure L(dB) represents the mean level of RMS value for the linear system normalized by the mean level of RMS value for the linear system without nonlinear dependence in both stiffness and damping, The value is calculated in decibel over the whole amplitude range $A \in [0, 10\,000]$ N. The best attenuation (up to 21 dB mean average attenuation) is obtained for the NES with highest mass and lowest damping. Here again, the attenuation becomes more smooth and regular for $\epsilon > 1\%$

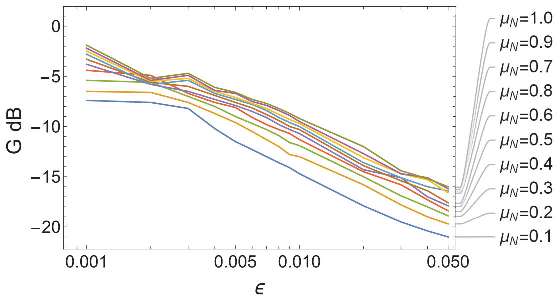

Figure 19: Best average gain obtained for various NES linear damping.

All these regular curves in logarithmic plots results suggest, except for the lowest values of ϵ, a dependence of the parameters as function of powers of ϵ and μ_N. The identification conduced on the whole data set leads to the following results:

$$\mathrm{G_{dB}} \approx C_G \cdot \epsilon^{1/3}\mu_N^{-1/6}, C_G \approx -43.1 \tag{52}$$
$$K_N \approx C_K \cdot \epsilon^{3/2}\mu_N^{1/3}, C_K \approx 35150 \tag{53}$$
$$\nu_N^a \approx \nu_N^c \approx C_\nu \cdot \epsilon^3\mu_N^{-1}, C_\nu \approx 2.5.10^7 \tag{54}$$
$$\delta_N \approx C_\delta \cdot (1+\alpha_1\epsilon+\alpha_2\epsilon^2)(1+\beta_1\mu+\beta_2\mu^2), \tag{55}$$

with for $0.001 \leq \epsilon < 0.009$, $C_\delta \approx 0.063$, $\alpha_1 \approx 3329.5$, $\alpha_2 \approx -228301$, $\beta_1 \approx -1.2$ and $\beta_2 \approx 0.47$ and for $0.009 \leq \epsilon \leq 0.05$, $C_\delta \approx 0.77$, $\alpha_1 \approx -11.5$, $\alpha_2 \approx -1441.1$, $\beta_1 \approx -1.3$ and $\beta_2 \approx 0.65$.

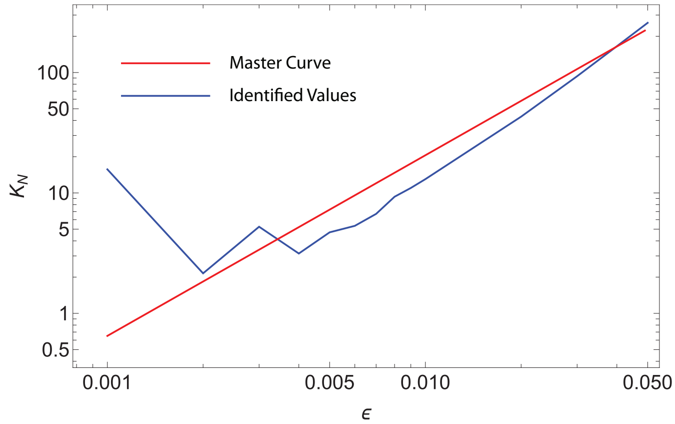

Figure 20: Comparison of a master curve and the identified values for K_N vs ϵ for $\mu_N = 0.2$

An example of comparison of a master curve and the identified values for K_N vs ϵ for $\mu_N = 0.2$ is given in Figure 20. Except ϵ lowest values, where the strongest fluctuations had been observed, the results are satisfactory and at least sufficient to give an estimate to more refined calculations.

6 Conclusion

This work was dedicated to the vibration mitigation of a simplified model of a FOWT by a NES with both linear and nonlinear stiffness and damping. We have shown that tuning NES nonlinear viscous damping allows to completely eliminate the detached resonances of the system and to keep absorber capacity to strongly limit the vibrations of the wind turbine over its whole operating range.

Furthermore, we have shown that classical tools of nonlinear dynamics (fixed points, SIM) can easily take into account this type of nonlinear damping and conduct fast analytical studies. We have shown that most of the dynamic of the system is conserved when nonlinear damping is added to the system. In particular, the fixed points of the principal frequency response curve are marginally modified when nonlinear damping is added to destroy detached resonances. Most of the influence of the nonlinear damping was observed on the SIM which shape remains mostly unaltered when nonlinear damping is accounted for, except its stability and for the particular values ν_N^0 that cancel the SIM at the bifurcation point $Z_2^{(1)}$. But, for the case under consideration in the present work with very small damping, $Z_2^{(1)}$ remains very close to zero and this property is not of particular interest. Nevertheless, for higher values of primary system damping this could be a useful feature.

By using a two steps optimization procedure we were able to define parameters that strongly limit the vibration of the simplified model of FOWT over its whole excitation range and a significant frequency range. The first step consists in imposing zero initial condition and optimize linear and cubic stiffness for various NES mass and linear damping by minimizing the FOWT ridge curve over its whole excitation range. The second step consists in, after computation of optimal parameter, estimating the nonlinear damping of the NES that cancel the detached resonance for the maximum amplitude.

The parametric study reveals that the parameter, say linear and nonlinear stiffness, attenuation and nonlinear damping depend upon simple power laws in NES mass and linear damping. This simple result is useful for NES dimensioning.

Bibliography

Abramson, H. N. (1955). "Response Curves for a System With Softening Restoring Force". *Journal of Applied Mechanics* 22, pp. 434–435. DOI: 10.1115/1.4011105

Alexander, N. A. and F. Schilder (2009). "Exploring the performance of a nonlinear tuned mass damper". *Journal of Sound and Vibration* 319, pp. 445–462. DOI: 10.1016/j.jsv.2008.05.018

Andersen, D., Y. Starosvetski, A. F. Vakakis, and L. Brergman (2012). "Dynamic instabilities in coupled oscillators induced by geometrically nonlinear damping". *Nonlinear Dynamics* 67, pp. 807–827. DOI: 10.1007/s11071-011-0028-0

Bakre, S. V. and R. S. Jangid (2007). "Optimum parameters of tuned mass damper for damped main system". *Structural Control and Health Monitoring* 14.3, pp. 448–470. DOI: 10.1002/stc.166

Bellet, R., B. Cochelin, P. Herzog, and P.-O. Mattei (2010). "Experimental study of targeted energy transfer from an acoustic system to a nonlinear membrane absorber". *Journal of Sound and Vibration* 329, pp. 2768–2791. DOI: 10.1016/j.jsv.2010.01.029

Chen, Y.-Y., Z.-C. Qian, W. Zhao, and C.-M. Chang (2020). "A magnetic Bi-stable nonlinear energy sink for structural seismic control". *Journal of Sound and Vibration* 473, p. 115233. DOI: 10.1016/j.jsv.2020.115233

Den Hartog, J. P. (1947). *Mechanical Vibrations, Third Edition*. McGraw-Hill Book Compagny

Ding, H. and L.-Q. Chen (2020). "Designs, analysis, and applications of nonlinear energy sinks". *Nonlinear Dynamics* 100, pp. 3061–3107. DOI: 10.1007/s11071-020-05724-1

Gendelman, O., L. Manevitch, R. M'Closkey, and A. F. Vakakis (2001). "Energy Pumping in Nonlinear Mechanical Oscillators: Part I—Dynamics of the Underlying Hamiltonian Systems". *Journal of Applied Mechanics* 68, pp. 34–41. DOI: 10.1115/1.1345524

Gendelman, O., T. Sapsis, A. F. Vakakis, and L. A. Bergman (2011). "Enhanced passive targeted energy transfer in strongly nonlinear mechanical oscillators". *Journal of Sound and Vibration* 330, pp. 1–8. DOI: 10.1016/j.jsv.2010.08.014

Gourc, E., G. Michon, S. Seguy, and A. Berlioz (2014). "Experimental Investigation and Design Optimization of Targeted Energy Transfer Under Periodic Forcing". Vol. 136. 2, pp. 021021-1–8. DOI: 10.1115/1.4026432

Gourc, E., G. Michon, S. Seguy, and A. Berlioz (2015). "Targeted Energy Transfer Under Harmonic Forcing With a Vibro-Impact Nonlinear Energy Sink: Analytical and Experimental Developments". *Journal of Vibration and Acoustics* 137, p. 031008. DOI: 10.1115/1.4029285

Habib, G., G. I. Cyrillo, and G. Kerschen (2018). "Isolated resonances and nonlinear damping". *Nonlinear Dynamics* 96, pp. 979–994. DOI: 10.1007/s11071-018-4240-z

Habib, G. and F. Romeo (2020). "Comparative Analysis of NES and TMD Performance via High-Dimensional Invariant Manifolds". *IUTAM Symposium on Exploiting Nonlinear Dynamics for Engineering Systems*. Ed. by I. Kovacic and S. Lenci. Cham", pages=143–153: Springer International Publishing

Huang, N. E., Z. Shen, S. R. Long, M. C. Wu, H. H. Shih, Q. Zheng, N.-C. Yen, C. C. Tung, and H. H. Liu (1998). "The empirical mode decomposition and the Hilbert spectrum for nonlinear and non-stationary time series analysis". *Proc. R. Soc. Lond. A.* 454, pp. 903–995. DOI: 10.1098/rspa.1998.0193

Liu, Y., A. Mojahed, L. A. Bergman, and A. F. Vakakis (2019). "A new way to introduce geometrically nonlinear stiffness and damping with an application to vibration suppression". *Nonlinear Dynamics* 96, pp. 1819–1845. DOI: 10.1007/s11071-019-04886-x

[SW] Loudet, L., *Application of Empirical Mode Decomposition to the detection of Sudden Ionospheric Disturbances by monitoring the signal of a distant Very Low Frequency transmitter* version 1, 2009. URL: https://sidstation.loudet.org/emd-en.xhtml

Pahn, T., R. Rolfes, J. Jonkman, and A. Robertson (2012). "Inverse Load Calculation of Wind Turbine Support Structures - A Numerical Verification Using the Comprehensive Simulation Code FAST: Preprint (Revised)". *53rd AIAA/ASME/ASCE/AHS/ASC Structures, Structural Dynamics, and Materials Conference* (Apr. 23–26, 2012). AIAA. Honolulu, Hawaii. DOI: 10.2514/6.2012-1735

Rauscher, M. (1938). "Steady Oscillations of Systems With Nonlinear and Unsymmetrical Elasticity". *Journal of Applied Mechanics* 5.4, A169–A177. DOI: 10.1115/1.4008875

AL-Shudeifat, M. A. (2014). "Highly efficient nonlinear energy sinks". *Nonlinear Dynamics* 76, pp. 1905–1920. DOI: 10.1007/s11071-014-1256-x

Starosvetsky, Y. and O. V. Gendelman (2008). "Attractors of harmonically forced linear oscillator with attached nonlinear energy sink. II: Optimization of a nonlinear vibration absorber". *Nonlinear Dynamics* 51, pp. 47–57. DOI: 10.1007/s11071-006-9168-z

Starosvetsky, Y. and O. V. Gendelman (2009). "Vibration absorption in systems with a nonlinear energy sink: Nonlinear damping". *Journal of Sound and Vibration* 324, pp. 916–939. DOI: 10.1016/j.jsv.2009.02.052

Wang, J., N. E. Wierschem, B. F. Spencer, and X. Lu (2015). "Track Nonlinear Energy Sink for Rapid Response Reduction in Building Structures". *Journal of Engineering Mechanics* 141, p. 04014104. DOI: 10.1061/(ASCE)EM.1943-7889.0000824

[SW] Wolfram Research, Inc., *Mathematica 13.0* version 13, 2021. URL: https://www.wolfram.com

Wu, Z., S. Seguy, and M. Paredes (2021). "Basic Constraints for Design Optimization of Cubic and Bistable Nonlinear Energy Sink". *Journal of Vibration and Acoustics* 144.2. DOI: 10.1115/1.4051548

Zuo, H., K. Bi, and H. Hao (2020). "A state-of-the-art review on the vibration mitigation of wind turbines". *Renewable and Sustainable Energy Reviews* 121, p. 109710. DOI: 10.1016/j.rser.2020.109710

Zuo, H. and S. Zhu (2022). "Development of novel track nonlinear energy sinks for seismic performance improvement of offshore wind turbine towers". *Mechanical Systems and Signal Processing* 172, p. 108975. DOI: 10.1016/j.ymssp.2022.108975